Supplemental Information

Fullerene-Decorated PdCo Nano-Resistor Network Hydrogen Sensors: Sub-Second Response and Part-per-Trillion Detection at Room Temperature

Tu Anh Ngo[a,*], Ashwin T. Magar[a], Minh T. Pham[a], Hoang M. Luong[a], George Larsen[b], Yiping Zhao[a], and Tho D. Nguyen[a,*]

[a] *Department of Physics and Astronomy, University of Georgia, Athens, Georgia 30602, USA.*

[b] *Hydrogen Isotope Science Group, Savannah River National Laboratory, Aiken, South Carolina 29808, USA.*

[*] *Corresponding author*

Correspondence to: anhngo@uga.edu (T. A. Ngo), ngtho@uga.edu (T. D. Nguyen).

KEYWORDS

electrical hydrogen gas sensor, PdCo composite, nanohole arrays, Fullerene C_{60}, Teflon AF

Table of Contents

S1. State-of-the-art Pd-based H_2 sensors

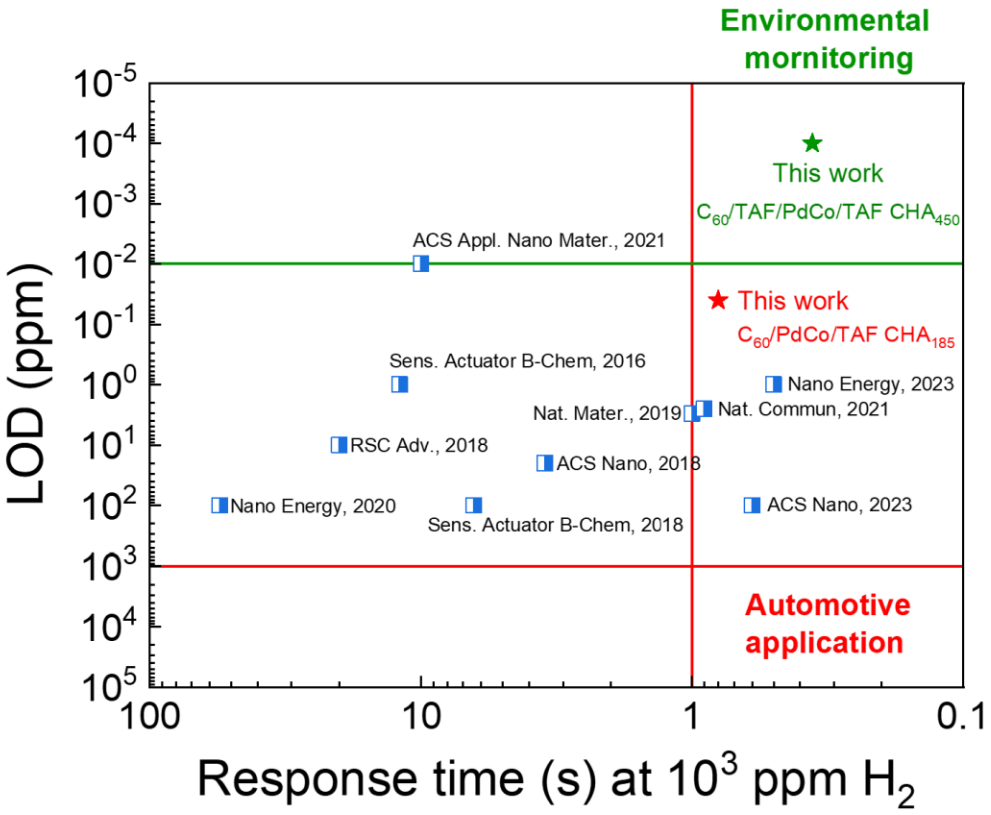

Figure S1. State-of-the-art Pd-based hydrogen gas sensors' sensing metrics. The response time and LOD requirements for automotive[1] and environmental mornitoring[2] applications are denoted in red and green lines, respectively.

Sens. Actuator B-Chem, 2016	Ref. [3]	Nano Energy, 2020	Ref. [4]
RSC Adv., 2018	Ref. [5]	ACS Appl. Nano Mater., 2021	Ref. [6]
ACS Nano, 2018	Ref. [7]	Nat. Commun, 2021	Ref. [8]
Sens. Actuator B-Chem, 2018	Ref. [9]	Nano Energy, 2023	Ref. [10]
Nat. Mater., 2019	Ref. [11]	ACS Nano, 2023	Ref. [12]

Table S1. Sensing metrics of electrical H_2 gas sensors operating at room temperature with either response time < 30 s at 1 mbar (or 0.1 vol.%) H_2 or LOD < 1000 ppm. n.a. = not addressed.

Device structure	Response time (s) (t_{90} if not specified)	Ambient pressure (mbar)	LOD (ppm - if not specified)	Sensor's hysteresis -free behavior	Resistance to poisoning gases	Ref.
C_{60}/PdCo/ Teflon AF/PMMA CHA_{185}	≤ 0.8	1	40 ppb	Yes	Yes	This work
C_{60}/Teflon AF/ PdCo/Teflon AF CHA_{450}	≤ 0.36	1	100 ppt			This work
PMMA-coated Pd-Co nanohole array	10.8	1	<0.01	Yes	Yes	6
Hollow Pd nanotube network (PVA@Pd8)	2.1	1	10	n.a.	Yes	13
Pd-Ni alloy thin films	t_{63} = 5	10	n.a.	n.a.	n.a.	14
Palladium nanowire engineered nanofiltration	13	1	1000	n.a.	n.a.	15
Ultrasmall grained Pd nanopattern	12	30	2.5	n.a.	n.a.	16
Pd-capped Mg film	6	10	1	n.a.	n.a.	17
Pd@Au core-shell nanoparticles	15	200	1000	n.a.	n.a.	18
Networks of ultrasmall palladium nanowires	~25	1	n.a.	n.a.	n.a.	19
Pd-decorated silicon nanomesh	t_{80} ~ 10	1	50	n.a.	n.a.	20
SiO2 nanorod coated-Pd	17	10	10	n.a.	n.a.	21
Pt-TiO2	10 ± 5	1	30	n.a.	n.a.	22
polyurethane@Pd	24	1	20	n.a.	n.a.	23
Pd nanowires	25	1	50	n.a.	n.a.	24
Pd NP/graphene	300	1	20	n.a.	n.a.	25
PdNi Nanogap	0.5	20	500	n.a.	n.a.	26
Discontinuous palladium films on Polyimide	5	40	5000	n.a.	n.a.	27

Pd nanorod	7	n.a.	1000	n.a.	n.a.	[28]
Pd nanoparticles	1.2	10	10^4	n.a.	n.a.	[29]
Pd nanoparticles coated Multi-Walled Carbon Nano Tubes	15	300	n.a.	n.a.	n.a.	[30]

1

S2. SEM and EDS elemental mapping images

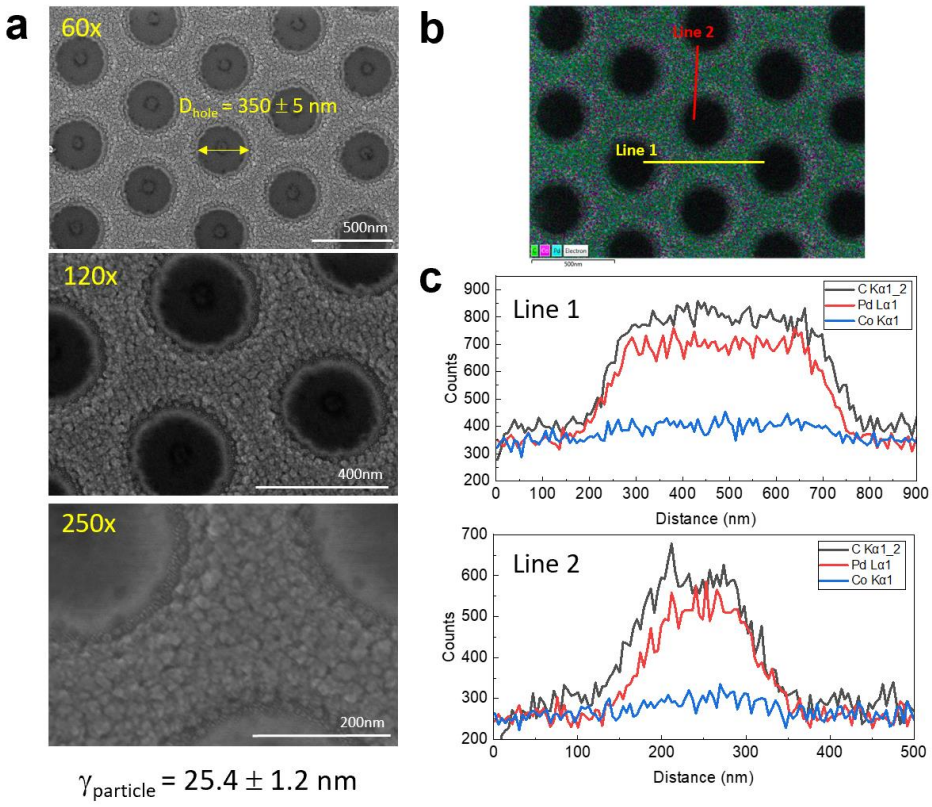

Figure S2. **(a)** SEM images of 20 nm C_{60}/5 nm PdCo CHA_{450} (hole diameter D_{hole} = 350 ± 5 nm) at different magnifications. The estimated diameter of the PdCo particles on the surface is $\gamma_{particle}$ = 25.4 ± 1.2 nm. **(b)** Energy-dispersive spectroscopy (EDS) elemental layered mapping. **(c)** EDS line spectra along two lines denoted in (b). Counts are based on weight percentages.

Table S2. Weight % to atomic % conversion table

Elements	Map (Fig. S2b)		Line 1 (Fig. S2c)		Line 2 (Fig. S2c)	
	Wt. %	At. %	Wt. %	At. %	Wt. %	At. %
C	79.5		7.15 ± 0.11		9.28 ± 0.13	
Pd	15.4	63	0.87 ± 0.02	67.7 ± 5.8	0.58 ± 0.02	62.8 ± 7.0
Co	5.1	37	0.24 ± 0.02	33.3 ± 2.9	0.19 ± 0.02	37.2 ± 4.1

S3. Hydrogen sensing characterization setups

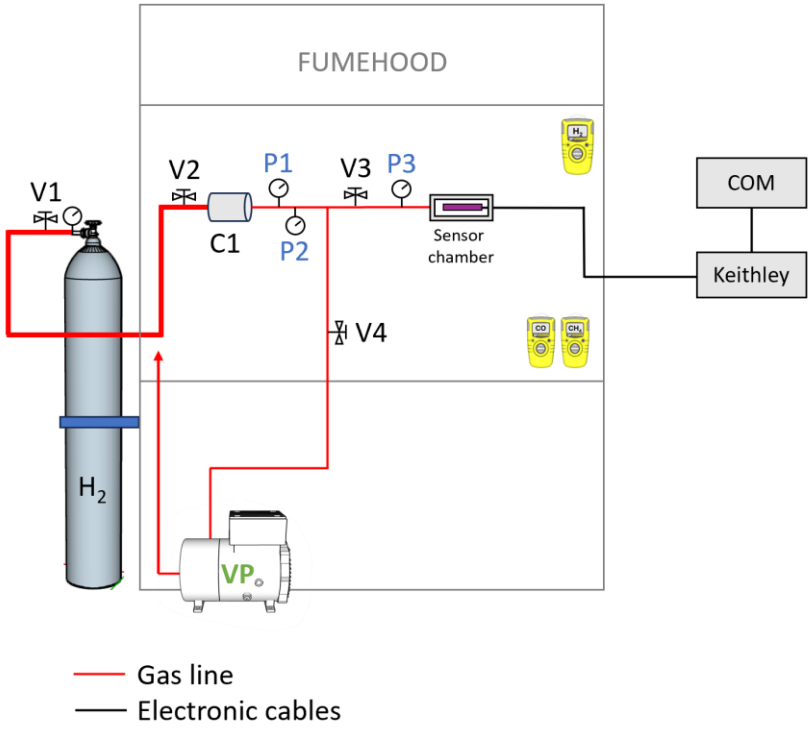

Figure S3. H_2 electrical sensing vacuum mode setup.

The vacuum mode set up is depicted in Figure S3. Different H_2 gas pressure in the sensor chamber can be prepared by recurringly diluting pure H_2 gas or the gas mixture of 4% H_2 in N_2 (Airgas) from chamber 1 (C1) to the sensor chamber by several gas valves (V1-V3). The H_2 pressures are monitored by three independent pressure transducers (two PX409-USBH, Omega and a Baratron, MKS). Finally, the chamber sensor is isolated to C1, and the gas inside the chamber is pumped out using valve V4 to achieve the base pressure of ~5 x 10^{-4} mbar in the chamber. The resistance of the sensors is recorded during the process using 4-point probe meaurement by a Keithley 2635B current source. In order to further exploring the measurement at a lower H_2 pressure, 4% or 100 ppm of H_2 mixed gas in N_2 balance can be used. In this case, we can prepare a mixture gas with H_2 pressure in sensor chamber down to 1 mbar, which is equivalent to partial hydrogen pressure/concentration of 40 ppm or 100 ppb, respectively. In order to probe at lower H_2

concentrations (a few ppb or ppt level), we will need to utilize further diluted H_2 gas as the gas source.

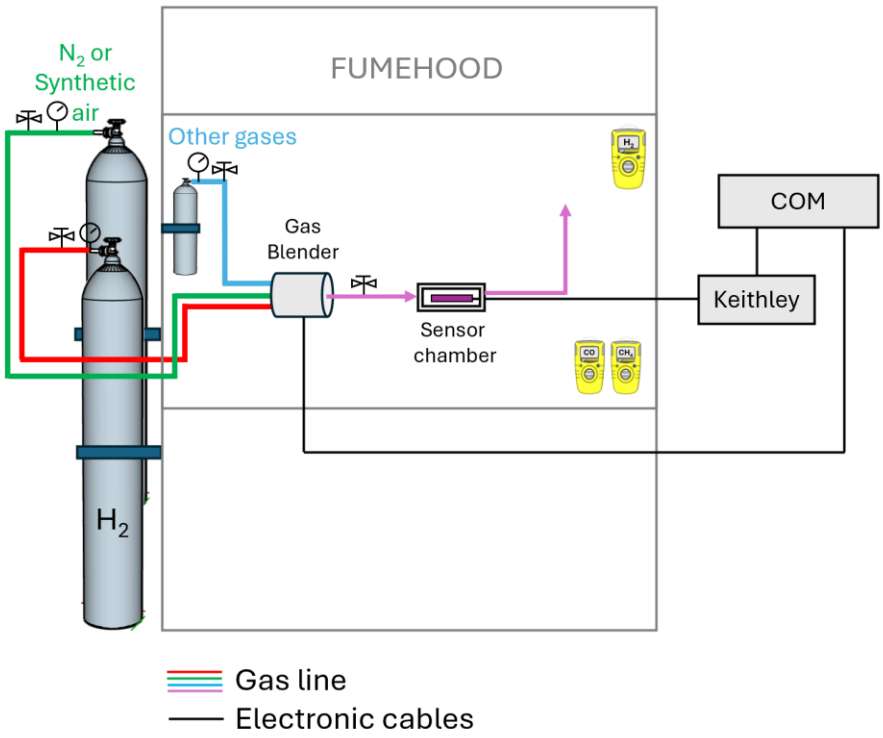

Figure S4. H_2 electrical sensing flow mode setup.

In addition to the vacuum mode setup, the gas sensing measurement is also performed in flow mode to mimic the leakage (Figure S4). 4% H_2 balance in N_2 are further diluted with ultra-high purity N_2 gas to the targeted concentrations ≤ 4 vol. % H_2 by a commercial gas blender (GB-103, MCQ Instruments). The gas flow rate is kept constant at 400 ml/min or 400 sccm at 1 atm for all measurements. The gas cell and gas outlet are placed inside a fume hood during the measurement.

S3. Sensing characteristics of PdCo thin films

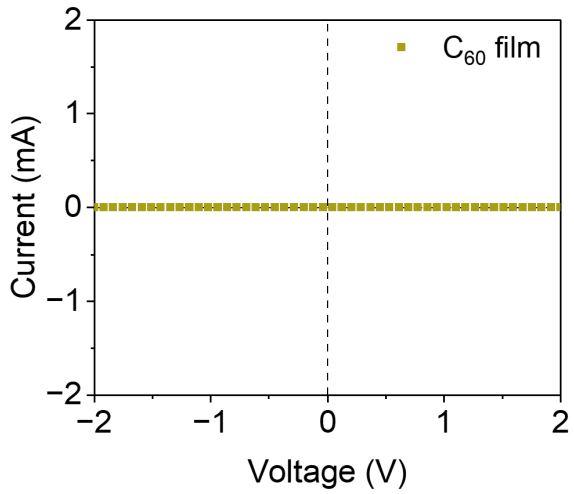

Figure S5. I-V characteristics of C_{60} film.

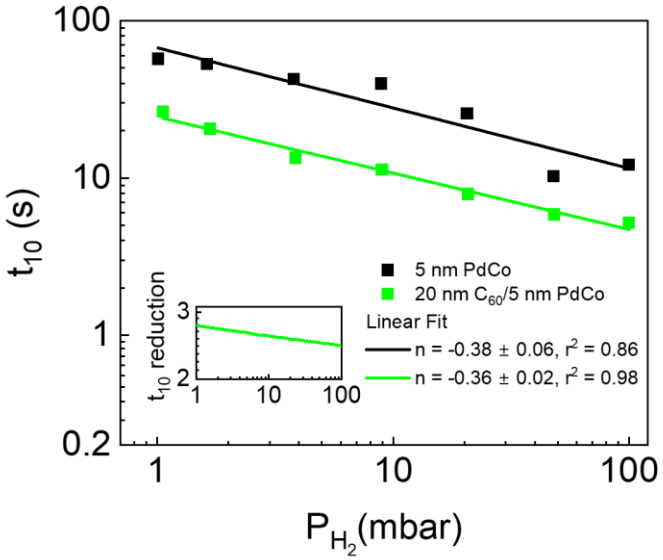

Figure S6. Desorption time t_{10} of 5 nm PdCo and 20 nm C_{60}/5 nm PdCo thin films.

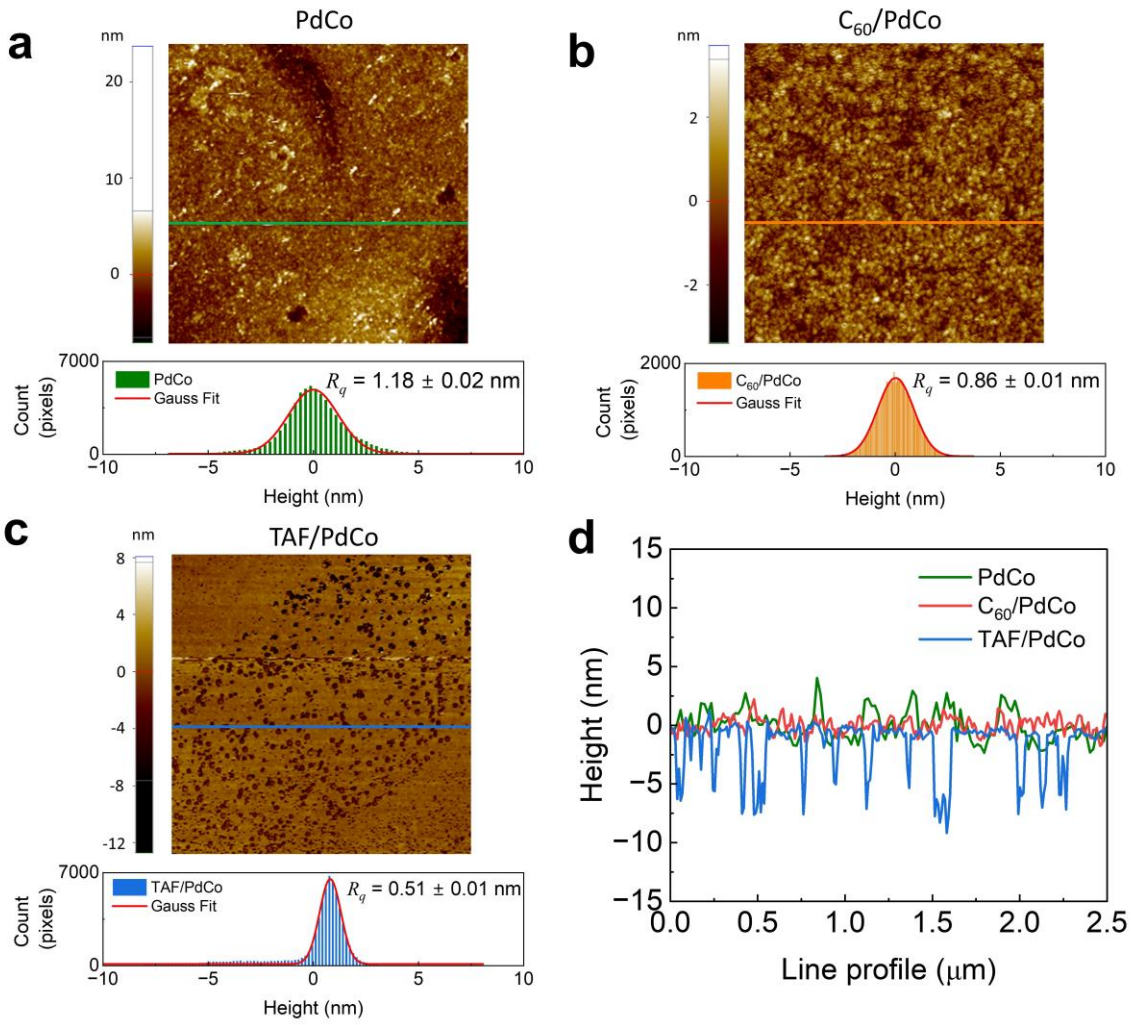

Figure S7. AFM images of 5 nm PdCo thin film on **(a)** a glass substrate, **(b)** a 50-nm C_{60}-coated glass subtrate, **(c)** a 30-nm TAF-coated glass substrate and the corresponding histograms. **(d)** The line profiles across the films extracted from figures (a-c).

1

S4. Sensing characteristics of CHAs on different C_{60} thicknesses

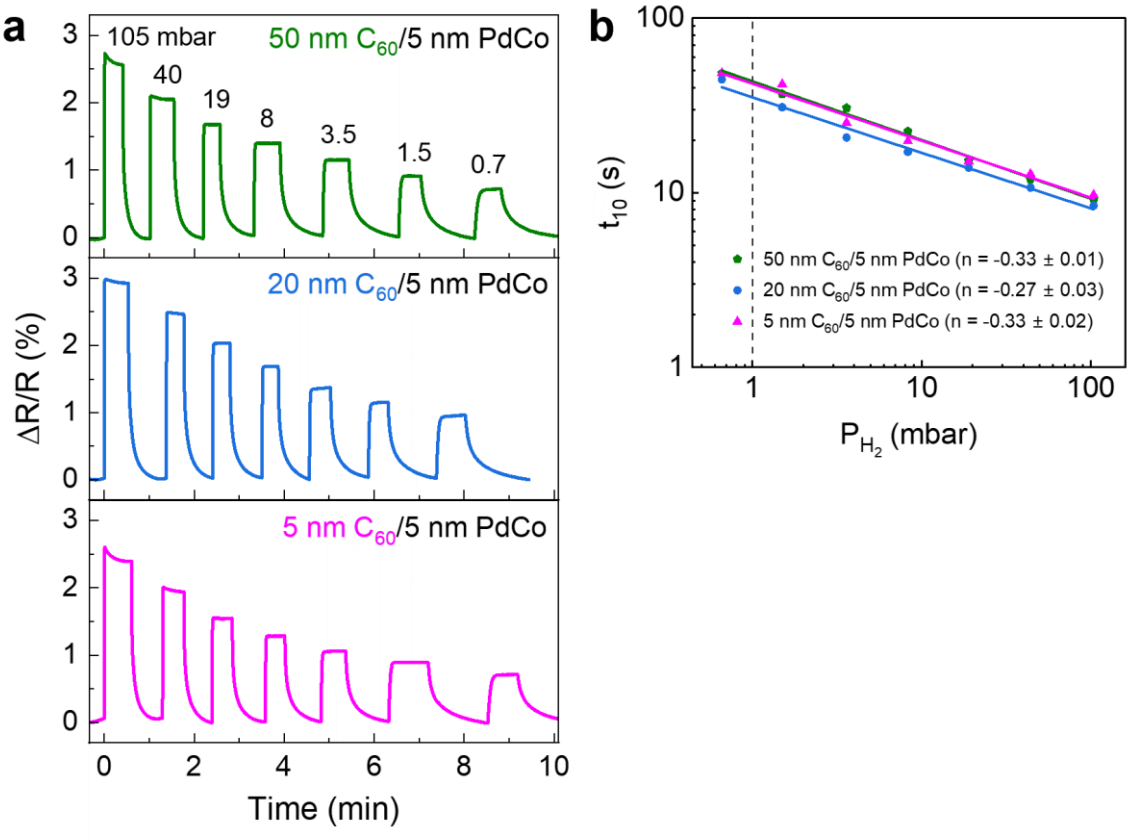

Figure S8. Sensing performances of C_{60}/5 nm PdCo CHA_{450} sensors with different C_{60} thicknesses. (a) Sorption dynamics in response to step wise decreasing H_2 pressure from 105 to 0.7 mbar. **(b)** Release time t_{10} extracted from (a). All measurements were performed in vacuum mode at room temperature.

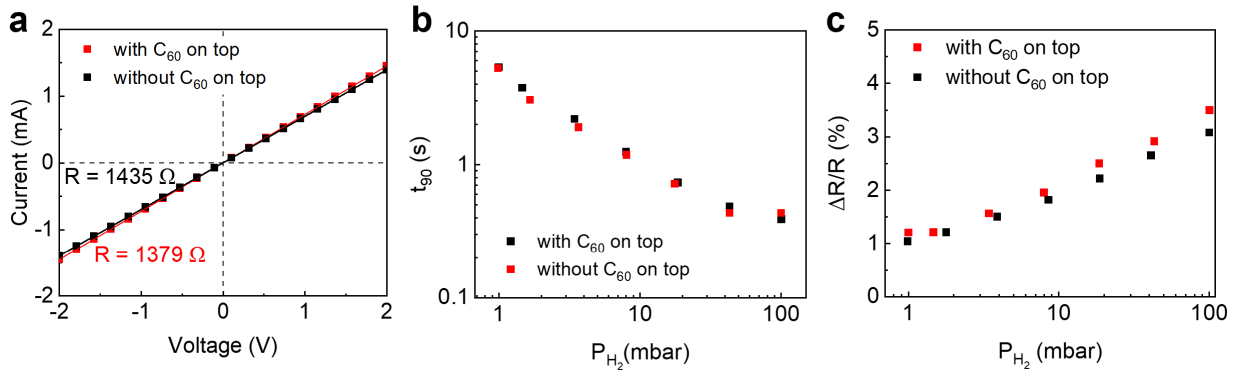

Figure S9. Sensing performances of 20 nm C_{60}/5 nm PdCo CHA_{300} sensors with and without 20 nm C_{60} on top. (a) I-V characteristics, **(b)** response time t_{90} and **(c)** sensitivity of the sensors in response to step wise decreasing H_2 pressure from 100 to 1 mbar. All measurements were performed in vacuum mode at room temperature.

1

S5. CHAs with different etching time t_{RIE}

S5.1. Morphology characterization and glancing angle deposition (GLACD) simulation

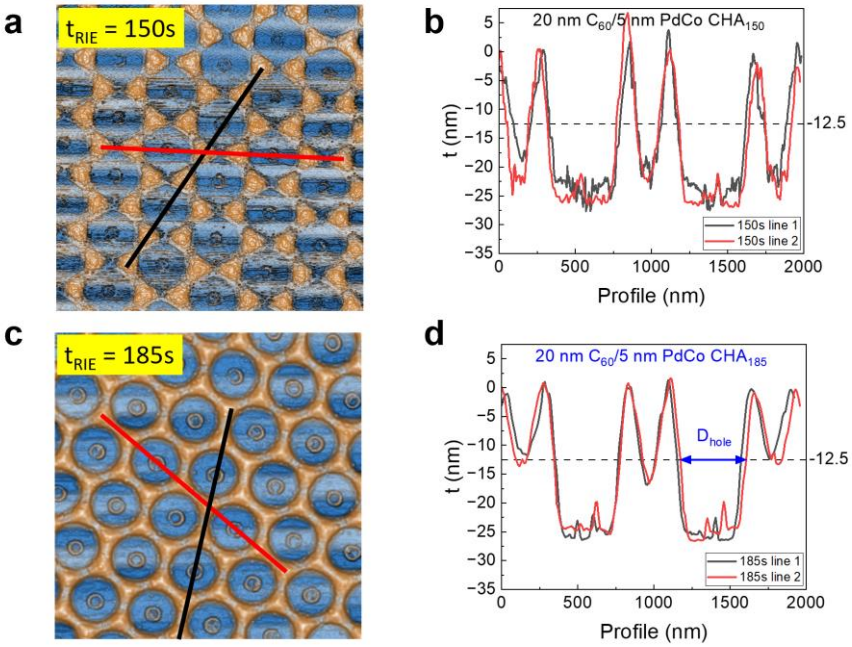

Figure S10. **(a)(c)** Top-view AFM image of CHA_{150} and CHA_{185} and **(b)(d)** the corresponding line profile along 2 lines denoted in (a)(c). The hole diameter D_{hole} is extracted from the middle of the hole and is averaged from 4 holes as depicted in (d).

When etching time < 160 s (Fig. S10 a&b), a nanotriangle array was achieved instead of a nanohole array due to the pronounced shadow effect from the big PS beads, resulting in a discontinuous nano network. The hole diameters of all CHAs were extracted from AFM line profiles (similar to CHA_{185} depicted in Fig. S10c&d) and summarized in Table S3. D_{hole} was then used as input parameters for GLACD simulation.[31]

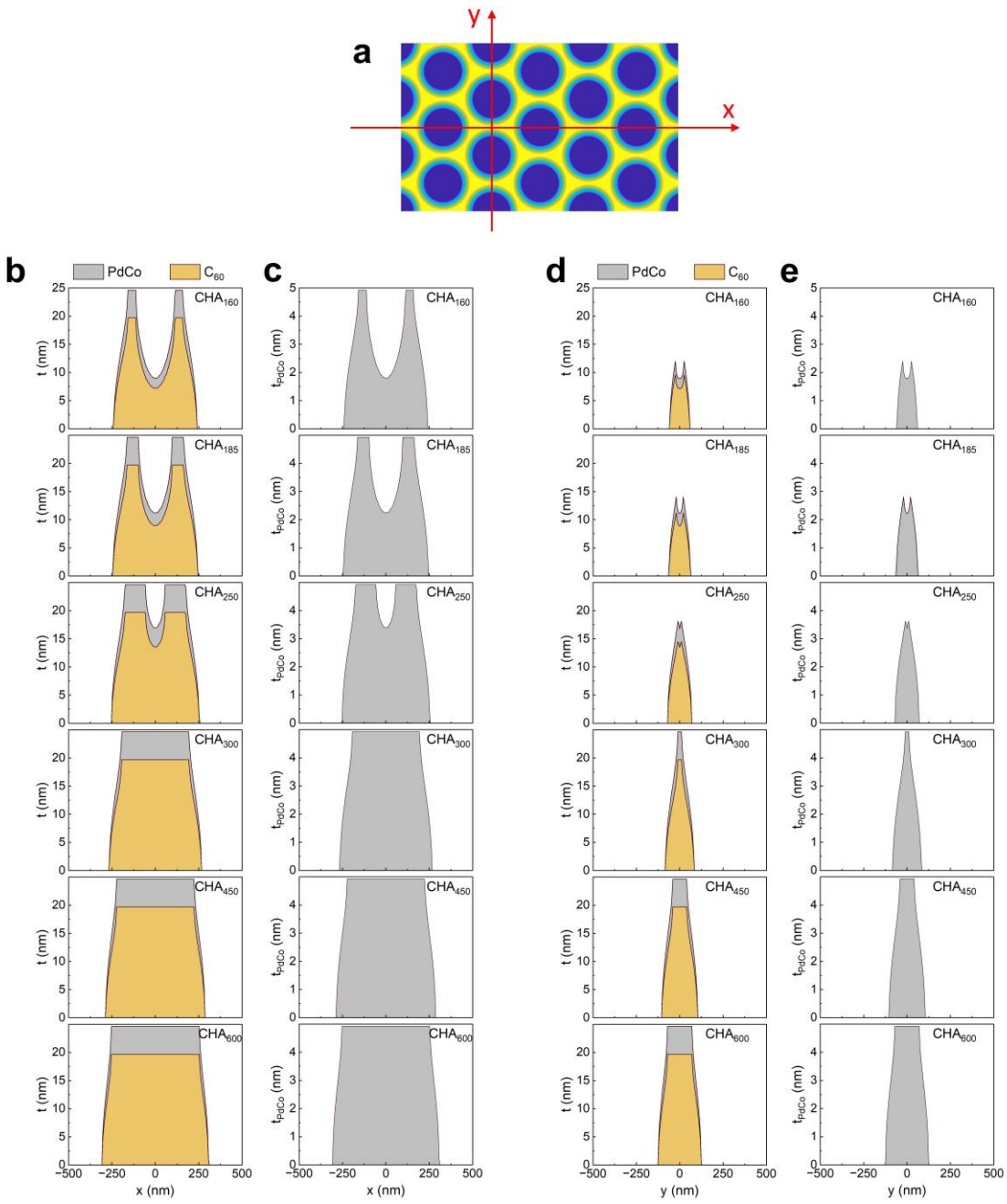

Figure S11. **(a)** Simulated hole array diagram and the bottleneck cross-section for each CHA_t along **(b)** the x-axis and **(d)** the y-axis denoted in (a). **(c)** and **(e)** are the thicknesses of the PdCo layer in (b) and (d) projected on a flat substrate.

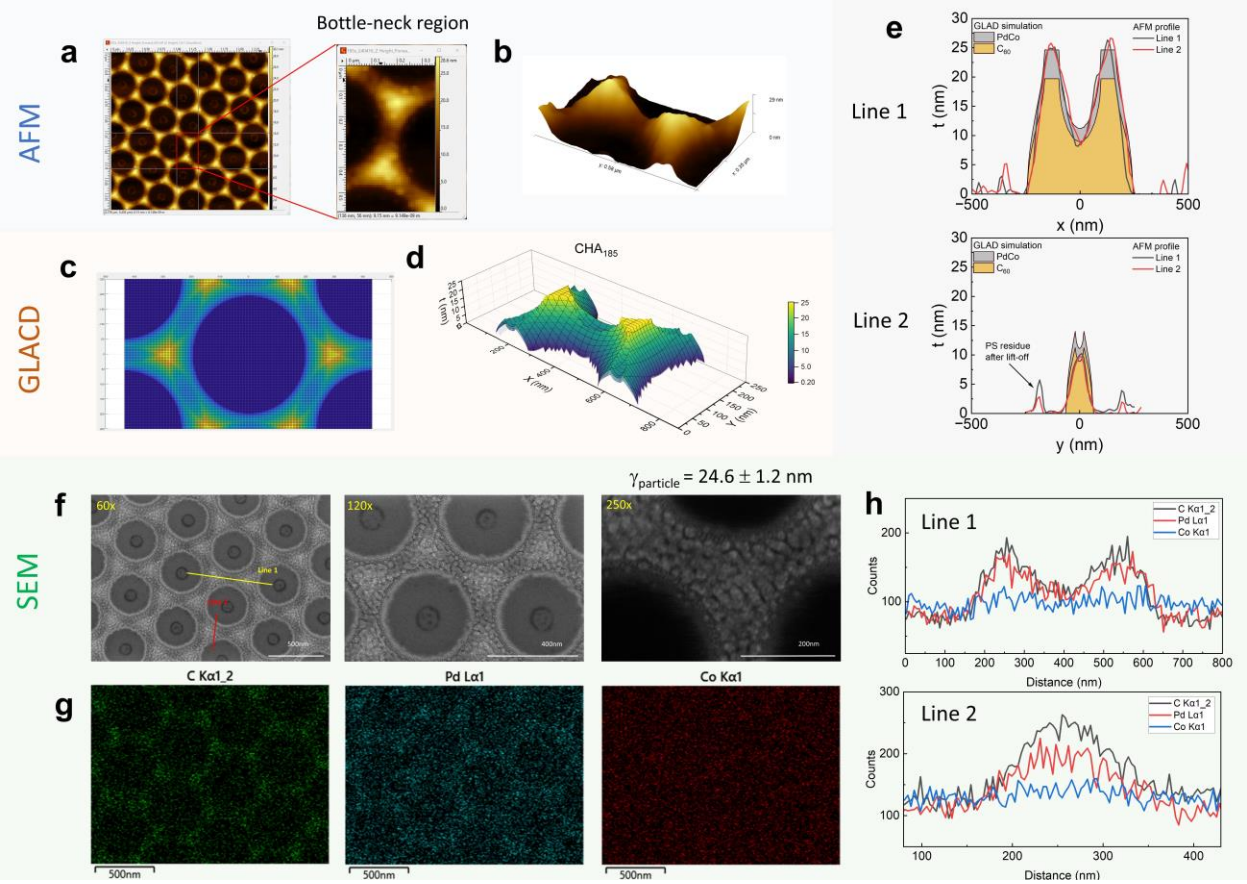

Figure S12. Comparison between GLACD simulation and data from AFM and SEM. (a) Top-view and **(b)** side-view AFM images of CHA_{185}. **(c)** Top-view and **(d)** side-view of CHA_{185} from GLACD simulation. **(e)** Line profiles along (line 1) and across (line 2) the bottle-neck region. **(f)** SEM images of 20 nm C_{60}/5 nm PdCo CHA_{185} at different magnifications. The estimated diameter of PdCo grains on the surface is $\gamma_{particle}$ = 24.6 ± 1.2 mm. **(g)** Energy-dispersive spectroscopy (EDS) elemental mapping. **(h)** EDS line spectra along (line 1) and across (line 2) the bottle-neck region denoted in (f). Counts are based on weight percentages.

S5.2. Surface-to-volume (SVR) ratio calculation

The morphology of each layer in CHAs was simulated using an in-house glancing angle deposition simulation.[31] The result of the simulation on the substrate for one unit cell is depicted in Fig. S12c with a resolution of 173 x 100 pixels^2. For polystyrene (PS) monolayer with a bead diameter of 500 nm, each pixel has a size of 5 x 5 nm^2. The color bar represents the thickness t of the deposited materials. The morphology of each layer can be illustrated as a 3D surface (Fig. S12d), and its surface area is calculated using *surfacearea* function in MATLAB.[32] The total surface area of PdCo layer can be calculated as

$$\text{Total PdCo surface} = \text{Top surface area of PdCo} + \text{Top surface area of } C_{60}. \quad \text{(S1)}$$

The volume of each layer is $V_{layer} = 5 \times 5 \times t$ (nm^3), thus the volume of PdCo layer is

$$V_{PdCo} = V_{total} - V_{C60}, \quad \text{(S2)}$$

Where V_{total} is total volume of the device C_{60}/PdCo and V_{C60} is volume of the C_{60} layer only. Finally, the surface-to-volume ratio is calculated as

$$\text{SVR} = \text{Total PdCo surface}/V_{PdCo}. \quad \text{(S3)}$$

Table S3. Summary of all parameters of 20 nm C_{60}/5 nm PdCo $CHA_{t_{RIE}}$ extracted from AFM images and GLACD simulations.

Etching time	Hole diameter	Bottle-neck width	Bottle-neck thickness of PdCo	Cross-sectional area	Bottle-neck length	Surface to volume ratio	Resistance	
t_{RIE}	D_{hole}	w	h_{PdCo}	$A_{bottleneck}$	l	SVR	$R_{without\ TAF}$	$R_{with\ TAF}$
s	nm	nm	nm	nm^2	nm	nm^{-1}	Ω	Ω
160	460 ± 3	40	2.00	1463.96	220	0.82	7062300	1889203
185	450 ± 4	50	2.46	1648.88	201	0.75	17744	15003
250	430 ± 8	70	3.55	2011.55	160	0.66	2835	2430
300	404 ± 2	96	4.92	2294.89	392	0.58	1503	1157
450	350 ± 5	150	4.92	2540.55	450	0.50	1093	1350
600	297 ± 6	203	4.92	2786.28	512	0.46	435	637

S5.3. Resistivity model

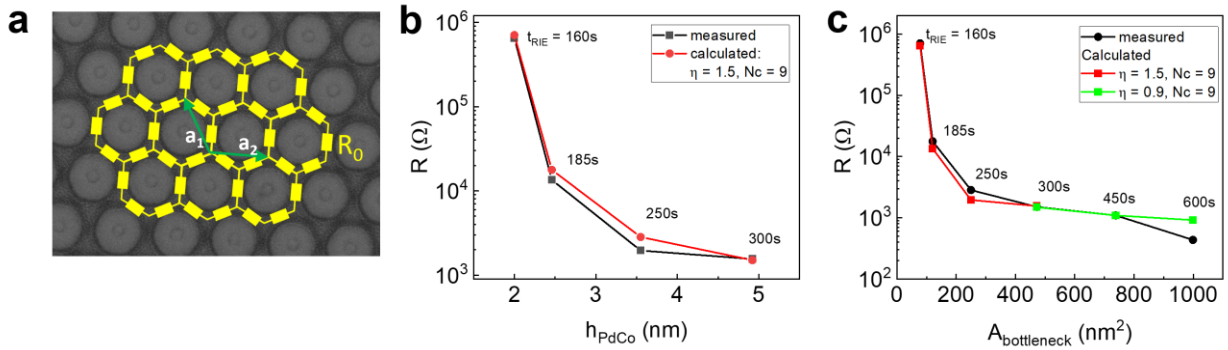

Figure S13. Resistivity model for 20 nm C60/5 nm PdCo $CHA_{t_{RIE}}$. (a) Schematic of the infinite two-dimensional hexagonal lattice of identical resistors R_0. **(b)(c)** Comparison between thickness-dependent resistance and Lacy's model (Ref. 7).

A hexagonal CHA structure can be considered as an infinite honeycomb resistor network of identical unit resistors (Fig. S13a); and its resistance R_{NH} is directly proportional to the elementary resistance R_0:

$$R_{NH} = NR_0, \tag{S4}$$

where the constant N is determined by

$$N = \frac{3}{4\pi^3}\int_{-\pi}^{\pi}\int_{-\pi}^{\pi}\frac{1-\cos(mx+ny)}{3-\cos(x)-\cos(y)-\cos(x+y)}dxdy\,. \tag{S5}$$

R_{NH}, here, is calculated spaced; the origin (0,0) and a given lattice point (m,n) of a two-dimensional hexagonal resistor network.[33] Since the clip test's pins using for 4-point-probe measurements are equally spaced, N should be a constant and has the same value for all devices. The effective resistance of the elementary resistor can be estimated by the following equation:

$$R_0 = \rho\frac{l}{w.h_{PdCo}} \tag{S6}$$

with ρ is the resistivity of PdCo alloy; l, w, and h_{PdCo} are the length, width, and thickness of PdCo layer (Table S2). Note that the value of the elementary resistance is determined solely by the intersection of the narrowest (w) and thinnest bottleneck region (h_{PdCo}).[6]

When the film thickness h_{PdCo} is smaller than the electronic mean free path in bulk l_{bulk}, the resistivity ρ is no longer a constant equal to the bulk resistivity ρ_0, but increases nonlinearly with the decrease of film's thickness. Lacy[34] had developed a general model that demonstrates the dependent of ρ on the film thickness, the surface roughness, and the grain boundary of the metallic thin film:

$$\rho = \frac{c\rho_0}{\kappa\prime(1-\ln(\kappa'))}, \tag{S8}$$

in which

$$\kappa' = \frac{t_{PdCo}-\eta}{2l_{bulk}}. \tag{S9}$$

In this model, c is a correction factor for the scattering from impurities in films ($c > 1$), and η is a thickness correction factor that accounts for the scattering from the surfaces, grain boundaries and surface roughness ($\eta < t_{PdCo}$). Thus, R_{NH} can be calculated using Lacy's model by substituting equations (S6 – S9) into (S4):

$$(R_{NH})_{calculated} = \frac{Nc}{\frac{t_{PdCo}-\eta}{2l_{bulk}}(1-ln\frac{t_{PdCo}-\eta}{2l_{bulk}})}\rho_0\frac{l}{wt_{PdCo}}. \tag{S10}$$

Using the values in Table S2 with fixed $l_{bulk} = 20$ nm and $\rho_0 = 6.72 \times 10^{-8}$ (Ωm), the thickness-dependent resistivities of $CHA_{t_{RIE}}$ (t_{RIE} = 160 s to 300 s) are shown in Fig. S13b. The theoretical model best fits experimental data when η = 1.5 nm and Nc = 9.0 for this regime. The small mismatch here could be explained by (i) the complexity of the CHA structure with non-uniformed film thickness and (ii) the assumption that the contribution of the triangle regions is negligible compared to the bottle-neck regions. For t_{RIE} > 300 s, t_{PdCo} remains unchanged, therefore R_{NH} was plotted versus the cross-sectional area of the bottleneck region in Fig. S13c with η = 0.9 nm and Nc = 9.0. Here, a smaller fitting parameter η than the ultra-thin film regime was used indicating that the scattering effects at the surface/grain boundaries/impurities is less serious in thicker films.

Overall, the non-linear dependency of CHAs' electrical resistance on the thickness or the bottleneck size being observed in the experiment was explained through Lacy's resistivity model.

S5.4. Sensing characteristics of CHAs with different etching time t_{RIE}

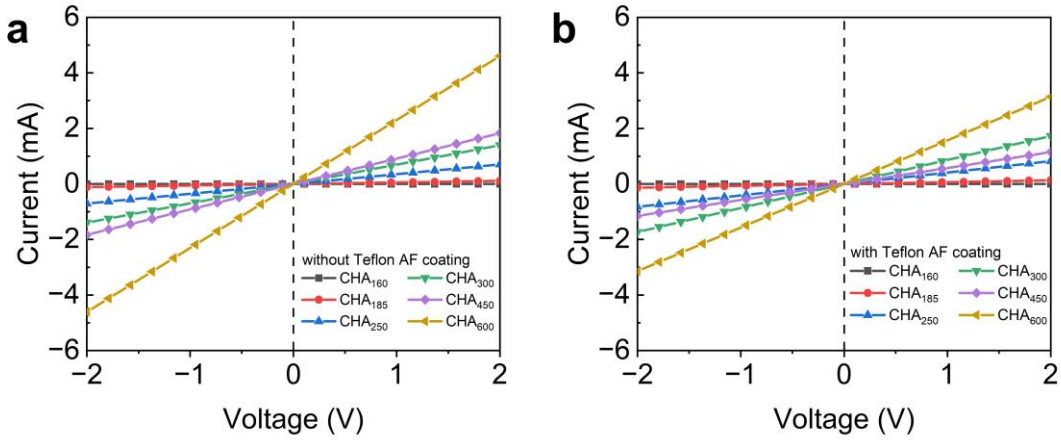

Figure S14. I-V characteristics of $CHA_{t_{RIE}}$ **(a)** without and **(b)** with TAF coating.

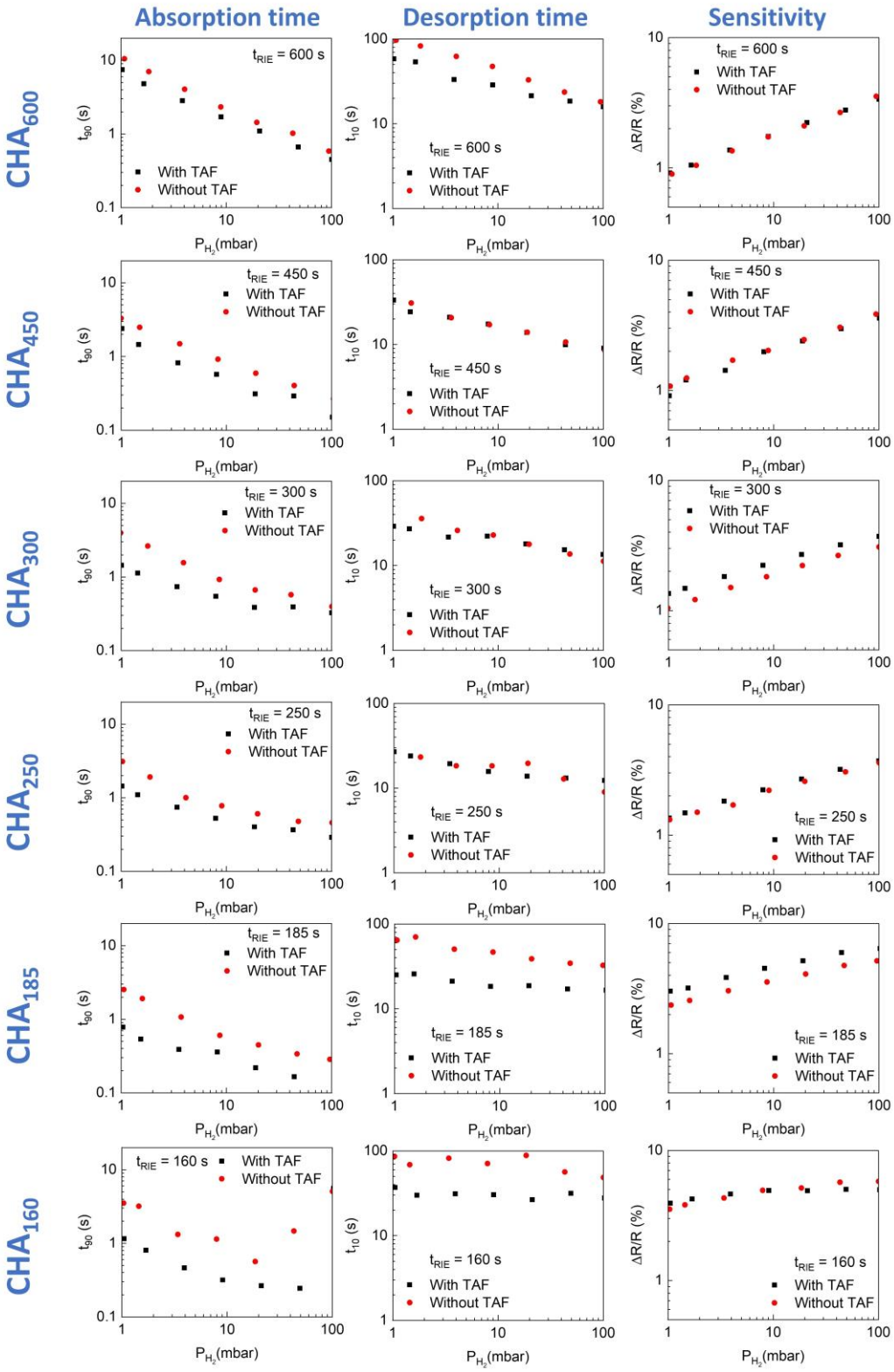

Figure S15. Absorption times, desorption times and sensitivities of 20 nm C_{60}/5 nm PdCo/(30 nm TAF) $CHA_{t_{RIE}}$ measured in vacuum mode at room temperature.

1

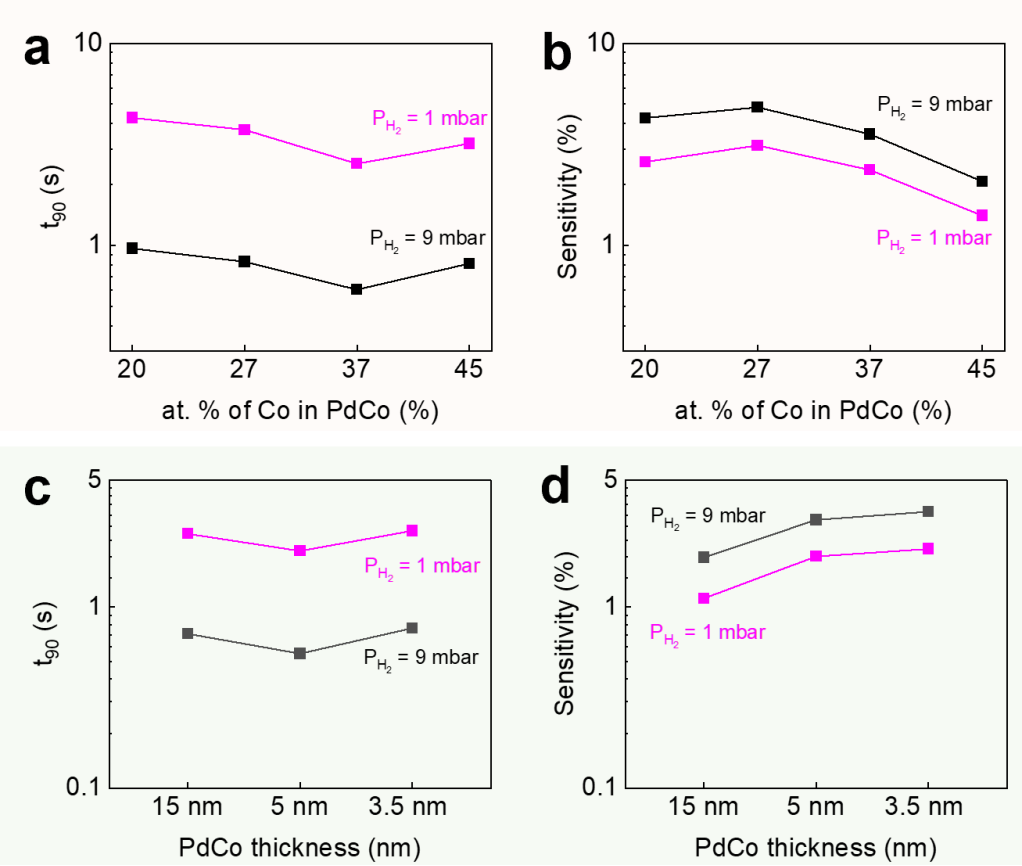

Figure S16. **(a-b)** Pd:Co composition-dependent and **(c-d)** PdCo thickness-dependent sensing performances of 20 nm C_{60}/PdCo CHA_{185}.

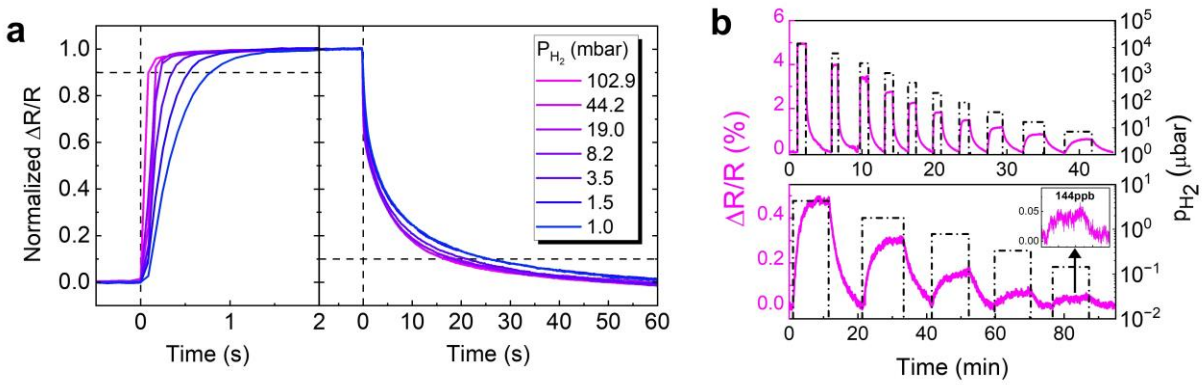

Figure S17. Sensing performances of 20 nm C_{60}/5 nm PdCo/30 nm TAF CHA$_{185}$. (a) Normalized absorption/desorption (left/right) kinetic of the sensor in response to varying H_2 pressure from 100 to 1 mbar measured at 12.2 Hz sampling frequency. **(b)** ΔR/R response to stepwise decreasing partial H_2 pressures of (top) 13880 – 7.2 µbar and (bottom) 4.32 – 0.144 µbar measured at 8.4 Hz sampling frequency. All measurements were performed in vacuum mode at room temperature.

1

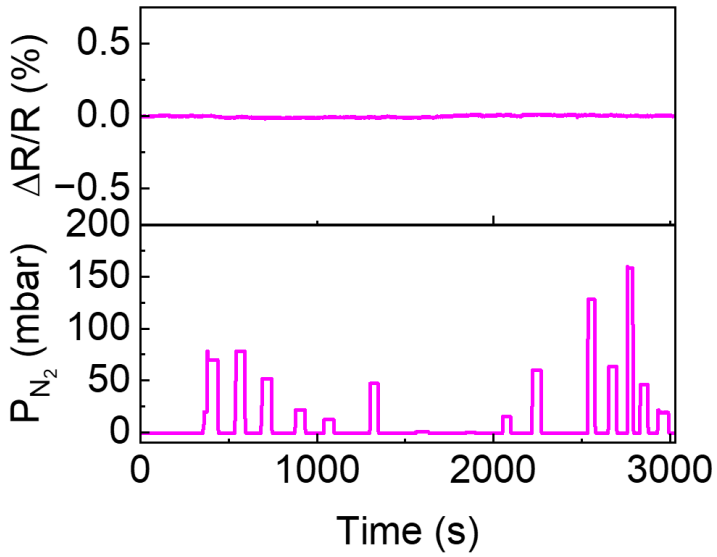

Figure S18. Controlled experiment of 20 nm C_{60}/3nm TAF/5 nm PdCo/30 nm TAF CHA$_{185}$ sensor with pure N_2. Top panel shows the sensor's response to the corresponding step-wise N_2 pressure pulses (from 0.1 to < 200 mbar) in the bottom panel. The experiment were performed in vacuum mode at room temperature and at sampling frequency $f_{sampling}$ = 12.2 Hz.

2

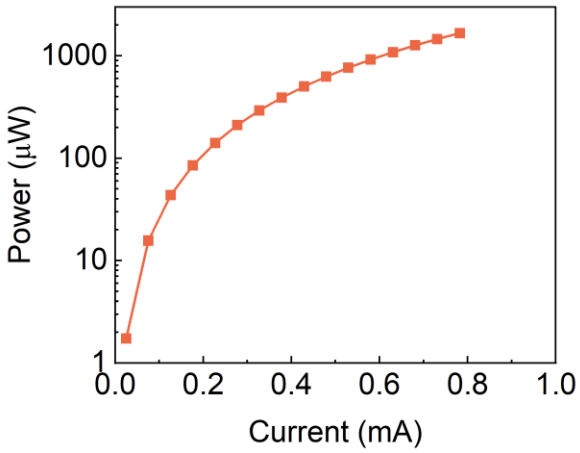

Figure S19. Measured power of the 20 nm C_{60}/3nm TAF/5 nm PdCo/30 nm TAF CHA_{450} sensor.

1

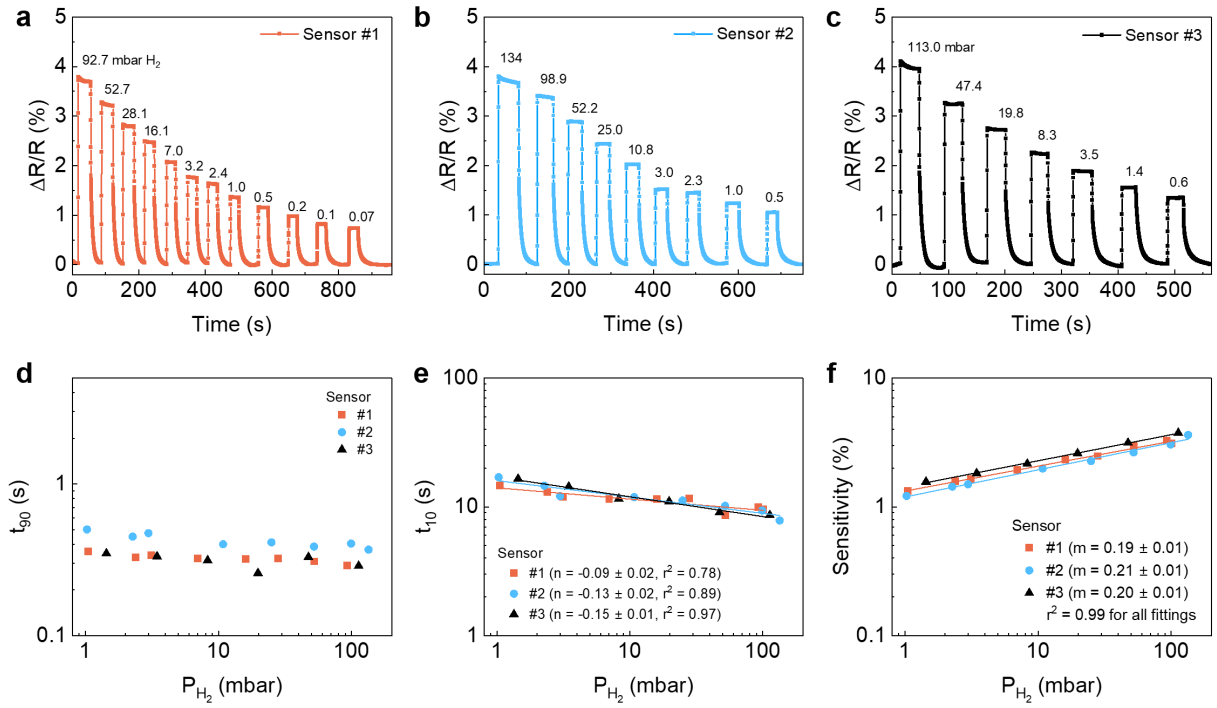

Figure S20. Sensing performances of 20 nm C_{60}/3nm TAF/5 nm PdCo/30 nm TAF CHA_{450} sensors. (a)(b)(c) ΔR/R responses of 3 sensors with the same device structure to stepwise decreasing H_2 pressures of ~100 to < 1 mbar ($f_{sampling}$ = 12.2 Hz). **(d)** Absorption time (t_{90}), **(e)** desorption time (t_{10}) and **(f)** sensitivity of the 3 sensors extracted from (a-c). All measurements were performed in vacuum mode at room temperature. Note that the data presented in Fig. S20 d&e are identical with the ones shown in the main text Fig. 6b.

2

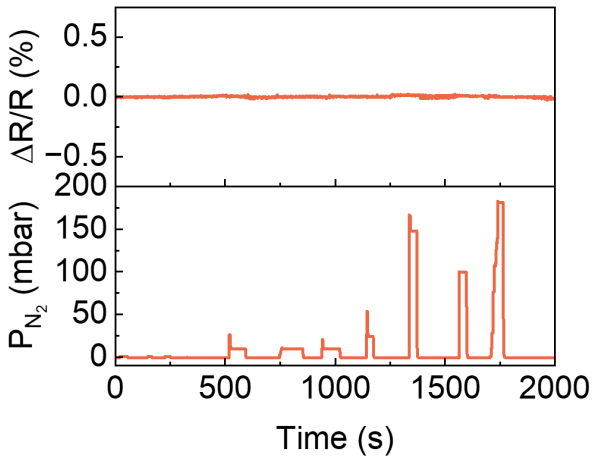

Figure S21. Controlled experiment of 20 nm C_{60}/3nm TAF/5 nm PdCo/30 nm TAF CHA_{450} sensor with pure N_2. Top panel shows the sensor's response to the corresponding step-wise N_2 pressure pulses (from 0.1 to < 200 mbar) in the bottom panel. The experiment were performed in vacuum mode at room temperature and at sampling frequency $f_{sampling}$ = 12.2 Hz.

1

S6. Noise evaluation

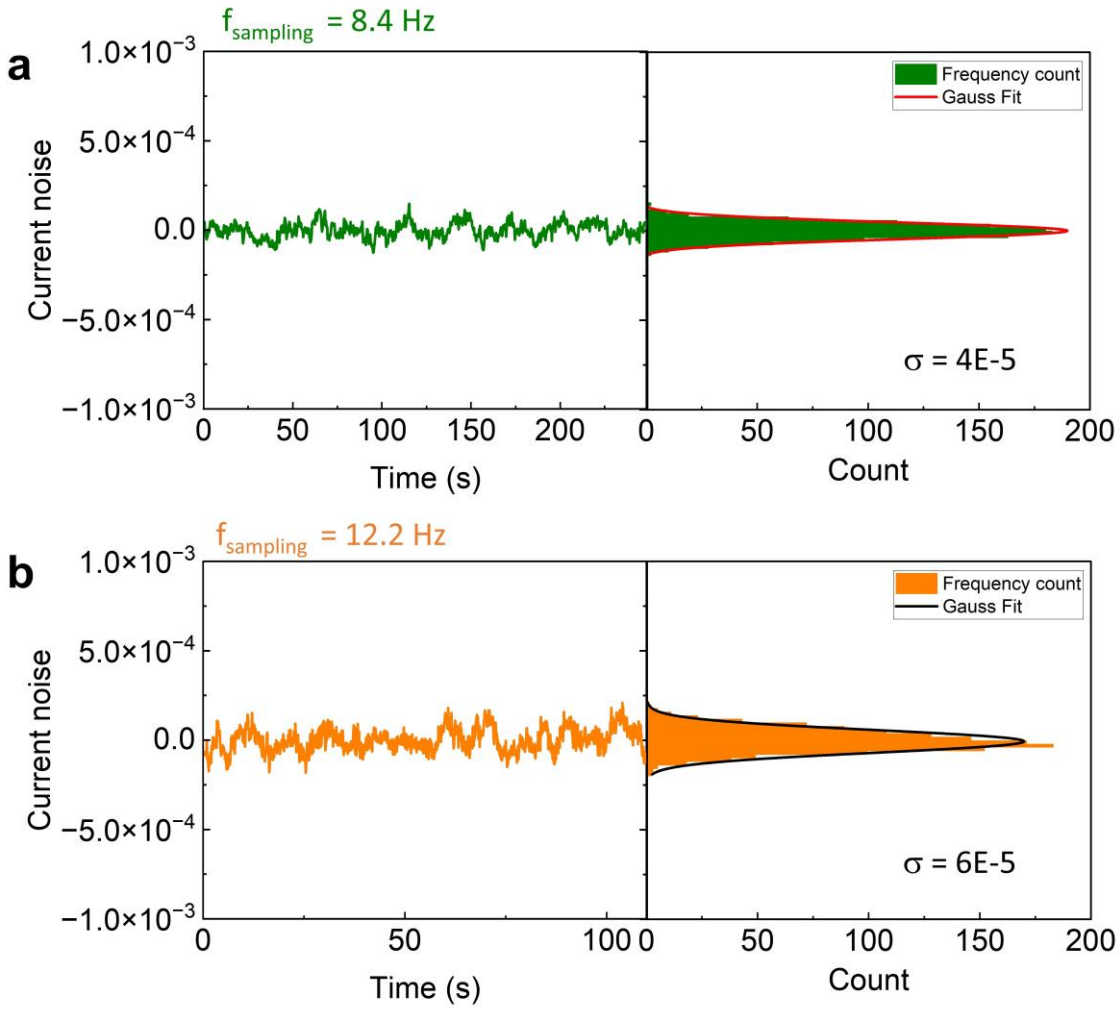

Figure S22. **(left panel)** Experimental current noise or resistance noise (defined as $\Delta I/I = \Delta R/R$) versus acquisition time of the 20 nm C_{60}/5 nm PdCo/30 nm TAF CHA_{185s} at different sampling frequency: **(a)** $f_{sampling}$ = 8.4 Hz and **(b)** $f_{sampling}$ = 12.2 Hz. ΔI is the fluctuation of the electric current around the equilibrium current, I. **(right panel)** Histogram plot of signal intensity. By definition, the LOD is 3σ with σ is the standard deviation extracted from the Gaussian Fits. Thus, at $f_{sampling}$ = 8.4 Hz, 3σ = 0.012%; and at $f_{sampling}$ = 12.2 Hz, 3σ = 0.018%.

S7. Interference gases and humidity tests

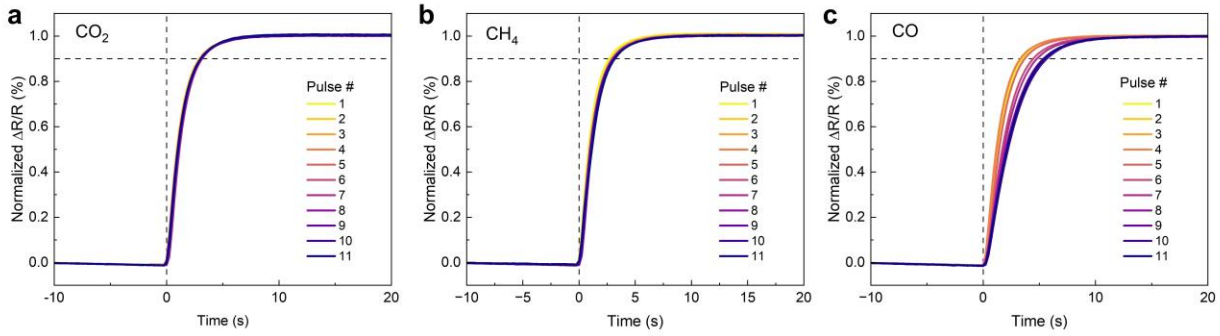

Figure S23. Normalized resistance dynamics of 20 nm C_{60}/5 nm PdCo/TAF/PMMA CHA_{450} sensor under the influence of interference gases extracted from Figure 6c. Pulses #1-3 and #9-11 are 2% H_2, and pulses #4-8 are a mixture of 2% H_2 and **(a)** 5% CO_2 or **(b)** 5% CH_4 or **(c)** 0.2% CO.

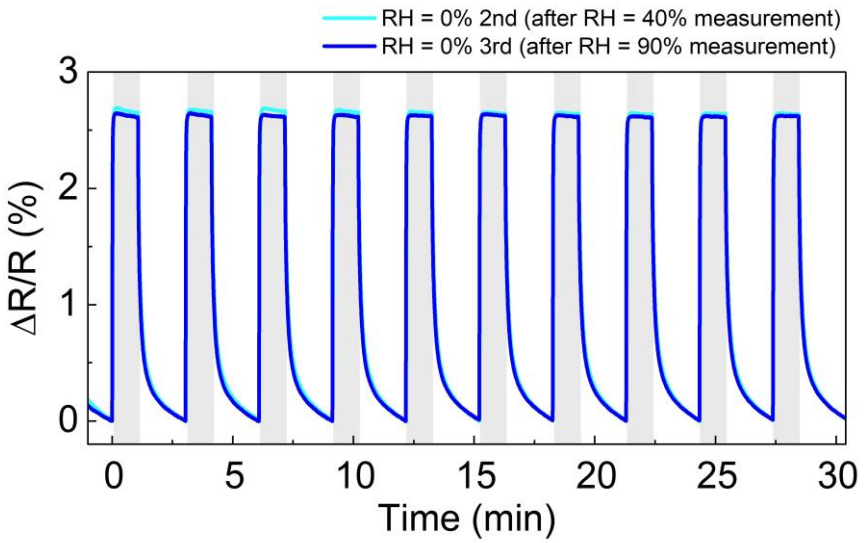

Figure S24. Time-resolved ΔR/R response of the 20 nm C_{60}/5 nm PdCo/TAF/PMMA CHA_{450} to 10 pulses of 2% H_2 with relative humidities (RH) of 0%, measured after the RH test.

S8. Pressure transducer's reaction time

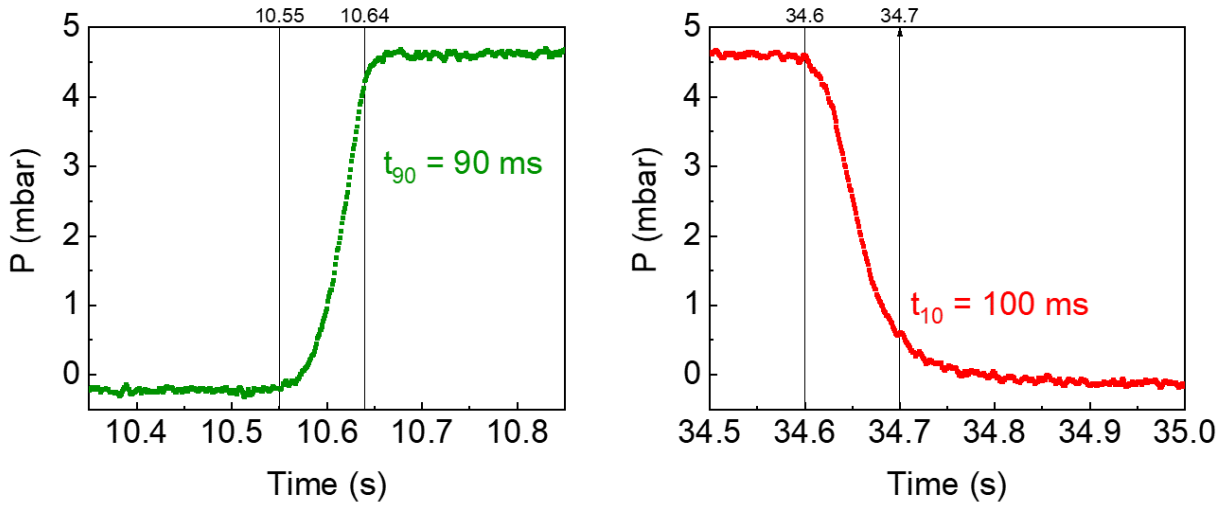

Figure S25. Reaction time of the pressure transducers while **(a)** loading and **(b)** unloading H_2 in the sensor chamber.

Supplementary references

1 Energy Efficiency and Renewable Energy (EERE), F. C. T. O. *Multi-Year Research, Development, and Demonstration Plan, 2011−2020. Section 3.7 Hydrogen Safety, Codes and Standards;*, <https://www.energy.gov/sites/prod/files/2015/06/f23/fcto_myrdd_safety_codes.pdf> (2015).

2 Energy Efficiency and Renewable Energy (EERE), E. E. a. R. E. *Funding Opportunity in Support of the Hydrogen Shot and a University Research Consortium on Grid Resilience*, <https://eere-exchange.energy.gov/Default.aspx?foaId=47252393-c846-4779-9760-86414eddda9f#FoaId47252393-c846-4779-9760-86414eddda9f> (2022).

3 Moon, J., Hedman, H.-P., Kemell, M., Tuominen, A. & Punkkinen, R. Hydrogen sensor of Pd-decorated tubular TiO2 layer prepared by anodization with patterned electrodes on SiO2/Si substrate. *Sensors and Actuators B: Chemical* **222**, 190-197 (2016). https://doi.org:https://doi.org/10.1016/j.snb.2015.08.054

4 Luong, H. M. *et al.* Bilayer plasmonic nano-lattices for tunable hydrogen sensing platform. *Nano Energy* **71**, 104558 (2020). https://doi.org:https://doi.org/10.1016/j.nanoen.2020.104558

5 He, J. *et al.* Integrating plasmonic nanostructures with natural photonic architectures in Pd-modified Morpho butterfly wings for sensitive hydrogen gas sensing. *RSC Advances* **8**, 32395-32400 (2018). https://doi.org:10.1039/c8ra05046e

6 Pham, M. T. *et al.* Pd80Co20 Nanohole Arrays Coated with Poly(methyl methacrylate) for High-Speed Hydrogen Sensing with a Part-per-Billion Detection Limit. *ACS Applied Nano Materials* **4**, 3664-3674 (2021). https://doi.org:10.1021/acsanm.1c00169

7 Nugroho, F. A. A., Darmadi, I., Zhdanov, V. P. & Langhammer, C. Universal Scaling and Design Rules of Hydrogen-Induced Optical Properties in Pd and Pd-Alloy Nanoparticles. *ACS Nano* **12**, 9903-9912 (2018). https://doi.org:10.1021/acsnano.8b02835

8 Luong, H. M. *et al.* Sub-second and ppm-level optical sensing of hydrogen using templated control of nano-hydride geometry and composition. *Nature Communications* **12**, 2414 (2021). https://doi.org:10.1038/s41467-021-22697-w

9 Lupan, O. *et al.* Ultra-sensitive and selective hydrogen nanosensor with fast response at room temperature based on a single Pd/ZnO nanowire. *Sensors and Actuators B: Chemical* **254**, 1259-1270 (2018). https://doi.org:https://doi.org/10.1016/j.snb.2017.07.200

10 Luong, H. M. *et al.* Ultra-fast and sensitive magneto-optical hydrogen sensors using a magnetic nano-cap array. *Nano Energy* **109**, 108332 (2023). https://doi.org:https://doi.org/10.1016/j.nanoen.2023.108332

11 Nugroho, F. A. A. *et al.* Metal–polymer hybrid nanomaterials for plasmonic ultrafast hydrogen detection. *Nature Materials* **18**, 489-495 (2019). https://doi.org:10.1038/s41563-019-0325-4

12 Jo, M.-S. *et al.* Ultrafast (~0.6 s), Robust, and Highly Linear Hydrogen Detection up to 10% Using Fully Suspended Pure Pd Nanowire. *ACS Nano* **17**, 23649-23658 (2023). https://doi.org:10.1021/acsnano.3c06806

13 Bi, S. *et al.* High-performance palladium nanotube network as fast, high-resolution, and wide range hydrogen detector in atmosphere. *Sensors and Actuators B: Chemical* **404**, 135307 (2024). https://doi.org:https://doi.org/10.1016/j.snb.2024.135307

14 Lee, E. *et al.* Hydrogen gas sensing performance of Pd–Ni alloy thin films. *Thin Solid Films* **519**, 880-884 (2010). https://doi.org:https://doi.org/10.1016/j.tsf.2010.07.122

15 Koo, W.-T. *et al.* Accelerating Palladium Nanowire H2 Sensors Using Engineered Nanofiltration. *ACS Nano* **11**, 9276-9285 (2017). https://doi.org:10.1021/acsnano.7b04529
16 Cho, S.-Y. *et al.* Ultrasmall Grained Pd Nanopattern H2 Sensor. *ACS Sensors* **3**, 1876-1883 (2018). https://doi.org:10.1021/acssensors.8b00834
17 Hassan, K. & Chung, G.-S. Fast and reversible hydrogen sensing properties of Pd-capped Mg ultra-thin films modified by hydrophobic alumina substrates. *Sensors and Actuators B: Chemical* **242**, 450-460 (2017). https://doi.org:https://doi.org/10.1016/j.snb.2016.11.078
18 Rajoua, K., Baklouti, L. & Favier, F. Electronic and Mechanical Antagonist Effects in Resistive Hydrogen Sensors Based on Pd@Au Core–Shell Nanoparticle Assemblies Prepared by Langmuir–Blodgett. *The Journal of Physical Chemistry C* **119**, 10130-10139 (2015). https://doi.org:10.1021/acs.jpcc.5b01636
19 Zeng, X. Q. *et al.* Hydrogen Gas Sensing with Networks of Ultrasmall Palladium Nanowires Formed on Filtration Membranes. *Nano Letters* **11**, 262-268 (2011). https://doi.org:10.1021/nl103682s
20 Gao, M., Cho, M., Han, H.-J., Jung, Y. S. & Park, I. Palladium-Decorated Silicon Nanomesh Fabricated by Nanosphere Lithography for High Performance, Room Temperature Hydrogen Sensing. *Small* **14**, 1703691 (2018). https://doi.org:10.1002/smll.201703691
21 Shim, Y.-S. *et al.* Nanogap-controlled Pd coating for hydrogen sensitive switches and hydrogen sensors. *Sensors and Actuators B: Chemical* **255**, 1841-1848 (2018). https://doi.org:https://doi.org/10.1016/j.snb.2017.08.198
22 Chen, W. P. *et al.* Extraordinary room-temperature hydrogen sensing capabilities of porous bulk Pt–TiO2 nanocomposite ceramics. *International Journal of Hydrogen Energy* **41**, 3307-3312 (2016). https://doi.org:https://doi.org/10.1016/j.ijhydene.2015.12.151
23 Chen, R., Ruan, X., Liu, W. & Stefanini, C. A reliable and fast hydrogen gas leakage detector based on irreversible cracking of decorated palladium nanolayer upon aligned polymer fibers. *International Journal of Hydrogen Energy* **40**, 746-751 (2015). https://doi.org:https://doi.org/10.1016/j.ijhydene.2014.11.026
24 Lim, S. H. *et al.* Flexible Palladium-Based H2 Sensor with Fast Response and Low Leakage Detection by Nanoimprint Lithography. *ACS Applied Materials & Interfaces* **5**, 7274-7281 (2013). https://doi.org:10.1021/am401624r
25 Chung, M. G. *et al.* Flexible hydrogen sensors using graphene with palladium nanoparticle decoration. *Sensors and Actuators B: Chemical* **169**, 387-392 (2012). https://doi.org:https://doi.org/10.1016/j.snb.2012.05.031
26 Lee, J., Shim, W., Lee, E., Noh, J.-S. & Lee, W. Highly Mobile Palladium Thin Films on an Elastomeric Substrate: Nanogap-Based Hydrogen Gas Sensors. *Angewandte Chemie International Edition* **50**, 5301-5305 (2011). https://doi.org:10.1002/anie.201100054
27 Kiefer, T., Villanueva, L. G., Fargier, F., Favier, F. & Brugger, J. Fast and robust hydrogen sensors based on discontinuous palladium films on polyimide, fabricated on a wafer scale. *Nanotechnology* **21**, 505501 (2010). https://doi.org:10.1088/0957-4484/21/50/505501
28 Villanueva, L. G. *et al.* Highly ordered palladium nanodot patterns for full concentration range hydrogen sensing. *Nanoscale* **4**, 1964-1967 (2012). https://doi.org:10.1039/C2NR11983H
29 Behzadi pour, G. & Fekri aval, L. Highly sensitive work function hydrogen gas sensor based on PdNPs/SiO2/Si structure at room temperature. *Results in Physics* **7**, 1993-1999 (2017). https://doi.org:https://doi.org/10.1016/j.rinp.2017.06.026

30 Han, M., Jung, D. & Lee, G. S. Palladium-nanoparticle-coated carbon nanotube gas sensor. *Chemical Physics Letters* **610-611**, 261-266 (2014). https://doi.org:https://doi.org/10.1016/j.cplett.2014.07.053
31 Ai, B. *Glancing angle deposition*, <http://ailabcqu.com/GLAD?_l=en>
32 Sartorius, S. *Surface area*, <https://www.mathworks.com/matlabcentral/fileexchange/62992-surface-area> (2024).
33 Wang, Y., Yang, F., Zhang, Z. & Zhao, Y. Performance of Transparent Metallic Thin Films. *The Journal of Physical Chemistry C* **125**, 16334-16342 (2021). https://doi.org:10.1021/acs.jpcc.1c04832
34 Lacy, F. Developing a theoretical relationship between electrical resistivity, temperature, and film thickness for conductors. *Nanoscale Research Letters* **6**, 636 (2011). https://doi.org:10.1186/1556-276x-6-636